Small-Signal Modeling and Damping Design of Unfolding-Based Single Stage AC-DC Converter Using the Extra Element Theorem

Dakota Goodrich*, Aditya Zade, Shubhangi Gurudiwan, Mahmoud Mansour, Regan Zane, and Hongjie Wang
Electrical and Computer Engineering Department, Utah State University
Logan, Utah – USA 84341
Email: *dakota.goodrich@usu.edu

***Abstract*—Unfolder-based quasi-single-stage ac-dc power converter has been widely used for high-power electric vehicle (EV) charging systems for its high efficiency and power density. However, the resonance between the grid inductance (impedance) and the capacitors on the soft-dc-link of the converter impacts the system stability and significantly limits the system control bandwidth and dynamic response performance. A quasi-single-stage ac-dc converter with unfolder plus T-bridge series resonant converter (T-SRC) is studied in this work. The small-signal modeling and plant transfer function derivation of the T-SRC is presented in this paper. A damping filter design using the extra element theorem (EET) is then proposed to achieve high-bandwidth and stable operation of the quasi-single-stage ac-dc converter. Simulation and hardware results from an 18 kW module for high-power EV charging are provided to validate the proposed modeling and damping filter design.**

***Index Terms*—Ac-dc converter, battery charger, extra element theorem (EET), grid-tied system, high-bandwidth control, T-type converter, unfolder, input filter, damping circuit.**

I. Introduction

Grid-tied ac-dc power converter is a key equipment for electric vehicle (EV) charging system and renewable energy integration. A two-stage ac-dc converter design with an active front-end stage for power factor correction (PFC) followed by a second dc-dc stage for output power control and isolation has been commonly used [1], [2]. To achieve higher efficiency and power density, a quasi-single-stage ac-dc converter with unfolder plus T-bridge series resonant converter (T-SRC) is studied in this work, similar to the unfolding-based topologies in [3]–[6]. The circuit topology of the converter studied in this paper is shown in Fig. 1 and consists of a three-phase grid connection with grid inductance (impedance), an unfolder, a T-type bridge, a series resonant tank, and active secondary bridge with battery load.

The back-to-back switches of the unfolder (Q_a, Q_b, Q_c) are operated at $2 \times f_{grid} = 120$ Hz and the unfolder diodes (D_{a1}, D_{b1}, D_{c1}, D_{a2}, D_{b2}, D_{c2}), as shown in Fig. 1, operate at grid frequency such that the most positive grid phase voltage is seen at the p-port, the most negative voltage is connected to the n-port, and the remaining phase is connected to the o-port. The T-SRC, which is introduced in [7], connects to the p-, o-, and n-ports with the soft-dc-link capacitors C_{po}, C_{on}, and C_{pn}. As detailed in [7], the T-SRC controls the PFC and output power with intermediate control variables $D_{p/n}$ and V_{1q}, respectively, where $D_{p/n}$ is calculated to control the ratio of input currents $I_{p/n} = I_p/I_n$, and V_1q is calculated for a given output current reference. These intermediate control variables are then used to calculate the modulation variables D_p, D_n, and D_ϕ, which are the duty cycle of the p-port and n-port bridges and the shift between the primary and secondary switching waveforms, respectively. Fig. 2 shows the large-signal waveforms governing the operation of the unfolder and T-SRC as a function of grid angle. Due to the low-frequency operation of the unfolder, the system exhibits a resonance between the grid inductance and the soft-dc-link capacitance of the T-SRC. This resonance has undesirable impacts on the system transfer functions and consequently on the closed-loop stability of the converter.

In [3], a resistor added in parallel with the grid inductance is used to dampen the resonance. Similarly, a network composed of two resistors and one capacitor is connected in parallel with the input inductance in [8]. However these approaches only work for low power applications where access to the physical inductor of the input filter is available. In high power applications that utilize the inherent grid inductance, the damping filter must be added in parallel to the entire input impedance, similar to the RC network proposed in [9]. This parallel passive damping approach is the chosen damping method for this application.

In [5], to address the input filter resonance and implement high-bandwidth control, an EET-based approach has been used to analyze the grid inductance to soft-dc capacitance resonance of an unfolder-based 21 kW ac-dc converter with a T-bridge, LCC resonant tank, and passive secondary diode bridge. However, it focuses on active damping control and the analysis cannot be easily applied to the T-SRC studied in this work due to different power converter topologies with different resonant tanks and secondary sides. In [7], the steady-state operation, modulation, and low-bandwidth control strategy of the T-SRC has been presented. However, the detailed small-signal modeling and high-bandwidth control are completely missing.

The key contributions of this paper include: (1) a detailed

This work is based in part upon work supported by the National Science Foundation (NSF) through the ASPIRE Engineering Research Center under Grant EEC-1941524 and CAREER Award under Grant 2239169.

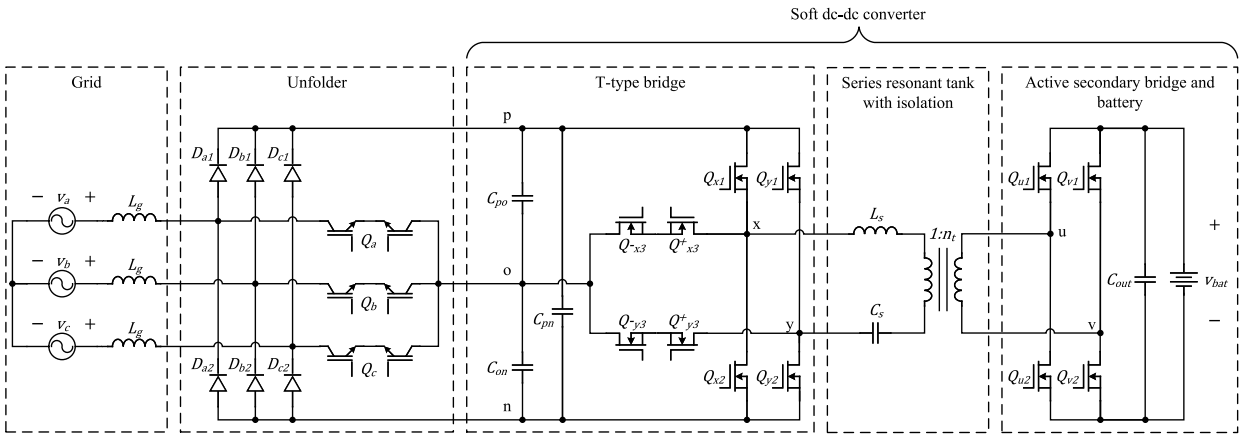

Fig. 1: Circuit diagram of the quasi-single-stage ac-dc converter with unfolder plus T-bridge series resonant converter (T-SRC).

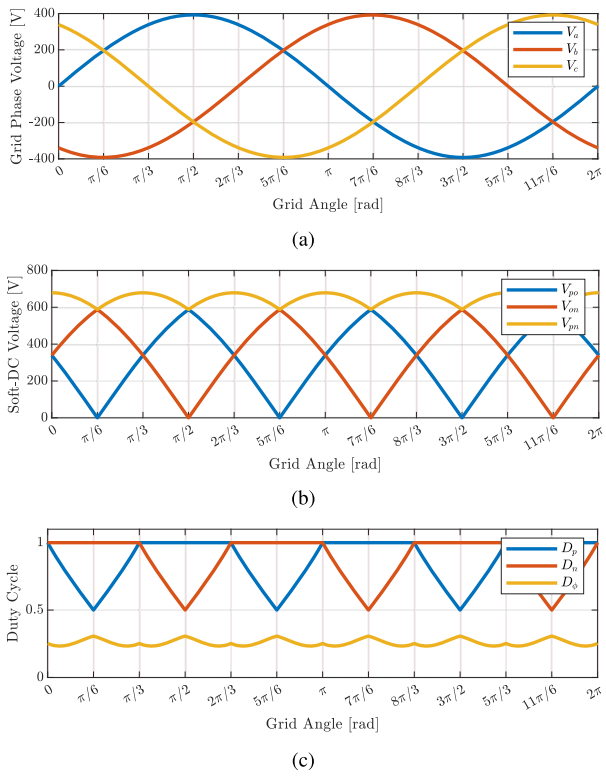

Fig. 2: Large-signal waveforms of the unfolder and T-SRC showing (a) grid voltages, (b) soft-dc-link voltages, and (c) duty cycles of the T-SRC as a function of grid angle.

small-signal modeling and analysis of a T-SRC with three critical open-loop transfer functions derived, (2) an investigation of stability issues caused by the grid inductance and soft-dc capacitors, and (3) a passive damping filter design using EET for achieving high-bandwidth control.

In this paper, Section II details the derivation of the small-signal model of the T-SRC and its use in finding three system transfer functions. Section III reviews the extra element theorem and utilizes the small-signal model to derive the EET impedances and analyze their impacts on the system transfer functions. Section IV describes the design of the chosen damping method to mitigate the effects of the resonance. Section V then validates the damping method with simulation and hardware results, and Section VI concludes the paper.

II. Small-Signal Modeling of T-Bridge Series Resonant Converter

A. Notation

Throughout this paper, the following conventions are used:

- Large-signal, steady-state quantities are denoted with capital letters, such as D_p.
- Small-signal quantities representing perturbations are denoted with lower-case letters and a "hat", such as $\hat{d}_p$.
- Phasor or complex quantities are represented with an arrow symbol, such as $\vec{s_p}$.
- If a perturbed quantity has a variable superscript, it indicates the variable that was perturbed to obtain that quantity, such as $\hat{i}^{\hat{d}_p}_{t,env}$, which indicates the perturbation in the envelope of the tank current I_t as a result of a perturbation in the duty cycle D_p.

B. Transfer Function Derivation

In this paper, the small-signal equivalent circuit of the T-SRC, which is the soft dc-dc converter as shown in Fig. 1, is first derived and presented in Fig. 3. Small signal phasor transformation and modeling approach for series resonant converters presented in [10], [11] has been utilized in this work to derive the small-signal equivalent circuit model.

From the derived small-signal equivalent circuit model, this paper derives three transfer functions of interest for which the EET was utilized. These are $\hat{i}_p/\hat{d}_p$, $\hat{i}_n/\hat{d}_n$, and $\hat{i}_{out}/\hat{d}_\phi$, as illustrated in Fig. 3. These functions were chosen because $\hat{i}_p/\hat{d}_p$ and $\hat{i}_n/\hat{d}_n$ most directly influence the PFC control loop, while $\hat{i}_{out}/\hat{d}_\phi$ most influences the output power control loop.

To derive these transfer functions, the fundamental harmonic approximation is used to derive switching functions $\vec{s_p}$, $\vec{s_n}$ and $\vec{s_s}$ as the complex transformation between the p-port, n-port,

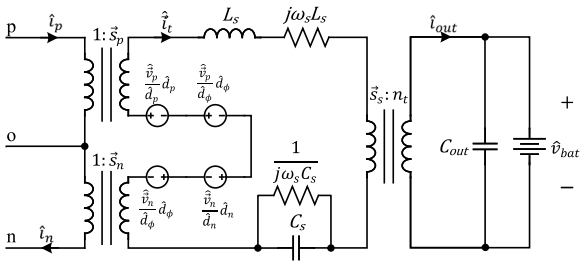

Fig. 3: Small-signal circuit diagram of T-SRC utilizing complex switching function transformers and phasor modeling of tank impedance.

and output port, respectively, with the resonant tank voltages and current. With the secondary active bridge duty cycle held at 50% and the secondary switching function taken as the reference angle, these are calculated as

$$\vec{s_p} = \frac{4}{\pi}\sin\left(\frac{\pi}{2}D_p\right)\angle\left(\pi D_\phi + \frac{\pi}{2}(1-D_p)\right), \tag{1}$$

$$\vec{s_n} = \frac{4}{\pi}\sin\left(\frac{\pi}{2}D_n\right)\angle\left(\pi D_\phi + \frac{\pi}{2}(1-D_n)\right), \tag{2}$$

$$\vec{s_s} = \frac{4}{\pi}\angle 0. \tag{3}$$

The tank voltages can be expressed as

$$\overrightarrow{V_{1p}} = V_p\vec{s_p}, \tag{4}$$

$$\overrightarrow{V_{1n}} = V_n\vec{s_n}, \tag{5}$$

$$\overrightarrow{V_{1s}} = V_{out}\frac{\vec{s_s}}{n_t}, \tag{6}$$

where n_t is the transformer turns ratio. By perturbing each respective duty cycle, the small-signal relationship between the p-port, n-port, and output port voltages and the three duty cycles can be found (e.g., $\hat{v_p}/\hat{d}_p$). These control-to-voltage responses are modeled as voltage sources in the small-signal circuit model. The resonant tank is also represented using the phasor transormation, which add complex-valued resistors in series and parallel with the tank inductor and capacitor, respectively. This small-signal ac equivalent circuit model shown in Fig. 3 allows the duty cycle-to-tank current transfer functions to be calculated using traditional circuit analysis, which can be separated into their envelope and phase responses (e.g., $\hat{i}_{t,env}^{d_p}/\hat{d}_p$ and $\hat{\theta}_t^{d_p}/\hat{d}_p$).

Next, using the complex switching functions, the time-domain response of the p-port, n-port, and output port currents are found as

$$\begin{aligned} I_p(t) &= I_t(t)\cdot s_p(t) \\ &= I_{t,env}\cos(w_s t+\theta_t)\cdot\Re\left(\vec{s_p}e^{jw_s t}\right), \end{aligned} \tag{7}$$

$$\begin{aligned} I_n(t) &= I_t(t)\cdot s_n(t) \\ &= I_{t,env}\cos(w_s t+\theta_t)\cdot\Re\left(\vec{s_n}e^{jw_s t}\right), \end{aligned} \tag{8}$$

$$\begin{aligned} I_{out}(t) &= I_t(t)\cdot\frac{s_s(t)}{n_t} \\ &= I_{t,env}\cos(w_s t+\theta_t)\cdot\frac{\Re\left(\vec{s_s}e^{jw_s t}\right)}{n_t}. \end{aligned} \tag{9}$$

By perturbing the duty cycles in the complex switching functions, the tank current envelope and phase are also perturbed. By linearizing these responses, the response due to changes in tank current envelope, tank current phase, and duty cycle (e.g., $\hat{i}_p^{d_p}/\hat{i}_{t,env}$, $\hat{i}_p^{d_p}/\hat{\theta}_t$, and $\hat{i}_p^{d_p}/\hat{d}_p$) are found.

Finally, the small-signal responses are combined to derive the transfer functions. The derived transfer functions are summarized as

$$\frac{\hat{i}_p}{\hat{d}_p} = \frac{\hat{i}_p^{d_p}}{\hat{i}_{t,env}}\frac{\hat{i}_{t,env}^{d_p}}{\hat{d}_p} + \frac{\hat{i}_p^{d_p}}{\hat{\theta}_t}\frac{\hat{\theta}_t^{d_p}}{\hat{d}_p} + \frac{\hat{i}_p^{d_p}}{\hat{d}_p}, \tag{10}$$

$$\frac{\hat{i}_n}{\hat{d}_n} = \frac{\hat{i}_n^{d_n}}{\hat{i}_{t,env}}\frac{\hat{i}_{t,env}^{d_n}}{\hat{d}_n} + \frac{\hat{i}_n^{d_n}}{\hat{\theta}_t}\frac{\hat{\theta}_t^{d_n}}{\hat{d}_n} + \frac{\hat{i}_n^{d_n}}{\hat{d}_n}, \tag{11}$$

$$\frac{\hat{i}_{out}}{\hat{d}_\phi} = \frac{\hat{i}_{out}^{d_\phi}}{\hat{i}_{t,env}}\frac{\hat{i}_{t,env}^{d_\phi}}{\hat{d}_\phi} + \frac{\hat{i}_{out}^{d_\phi}}{\hat{\theta}_t}\frac{\hat{\theta}_t^{d_\phi}}{\hat{d}_\phi} + \frac{\hat{i}_{out}^{d_\phi}}{\hat{d}_\phi}. \tag{12}$$

III. Extra Element Theorem Analysis and Simulation

A. Extra Element Theorem Introduction

The final result of the EET for a series-added element is

$$G_{new} = G_{old}\left(\frac{1+\dfrac{Z_{LC}}{Z_n}}{1+\dfrac{Z_{LC}}{Z_d}}\right) = \left(G|_{Z_{LC}=0}\right)G_{cf}\,, \tag{13}$$

where G_{new} and G_{old} are the transfer function with and without the extra element included, respectively, Z_{LC} is the impedance of the extra element, which for the present application is the parallel combined impedance of the grid inductance L_g and wye-reflected capacitance of the dc-link capacitors $C_\curlywedge$ ($= 3C_{po/on/pn}$), and Z_n and Z_d are the double null injection and single injection driving point impedances, respectively [5], [12]–[15]. The three impedances Z_{LC}, Z_n, and Z_d combine to define the correction factor G_{cf}. For an extra element to not significantly alter a desired transfer function, the correction factor must be near unity for all frequencies, which is accomplished when

$$\|Z_{LC}\| \ll \|Z_n\| \text{ and } \|Z_{LC}\| \ll \|Z_d\| \tag{14}$$

hold true at all frequencies. Using small-signal phasor modeling of the converter described below, Z_n and Z_d are calculated as

$$Z_n = \left.\frac{\hat{v}_{test}}{\hat{i}_{test}}\right|_{\text{output}\xrightarrow[\text{null}]{}0}, \tag{15}$$

and

$$Z_d = \left.\frac{\hat{v}_{test}}{\hat{i}_{test}}\right|_{\text{input}=0}, \tag{16}$$

where $\hat{v}_{test}$ and $\hat{i}_{test}$ are measured at the p-port or n-port, "output" is chosen from $\{\hat{i}_p, \hat{i}_n, \hat{i}_{out}\}$, and "input" is chosen from $\{\hat{d}_p, \hat{d}_n, \hat{d}_\phi\}$, depending on the transfer function of interest. It is important to note that Z_n and Z_d can be analyzed at either the p-port or n-port, due to the symmetric operation of the two ports. This is demonstrated in the symmetry of the plots in Fig. 5.

B. Calculation of Z_n

It is noteworthy to first explain that Z_n is infinite for all frequencies when the transfer function of interest is $\hat{i}_p/\hat{d}_p$ or $\hat{i}_n/\hat{d}_n$. This is because the output $\hat{i}_p$ or $\hat{i}_n$ corresponds with $\hat{i}_{test}$, which is nulled to zero when Z_n is measured at the p-port or n-port as shown in (15), respectively. On the other hand, Z_n is not necessarily infinite when the transfer function of interest is $\hat{i}_{out}/\hat{d}_\phi$. Therefore, analysis using small-signal phasor modeling was used to find the magnitude of Z_n at resonant frequency throughout the grid cycle, as measured at the p-port.

Firstly, the steady-state equation relating the input voltages (V_{po} and V_{on}) and complex tank voltages ($\overrightarrow{V_{1p}}$ and $\overrightarrow{V_{1n}}$) is perturbed with

$$V_{po} \rightarrow V_{po} + \hat{v}_{test} \text{ and } D_\phi \rightarrow D_\phi + \hat{d}_\phi, \tag{17}$$

and the result is linearized to

$$\begin{aligned}\frac{\hat{\overrightarrow{v}}_{1p}}{\hat{v}_{test}} =& \frac{4}{\pi}\sin\left(\frac{\pi}{2}D_p\right)e^{j\left(\pi D_\phi+\frac{\pi}{2}(1-D_p)\right)} \\ &+ \frac{\hat{d}_\phi}{\hat{v}_{test}}4V_{po}\sin\left(\frac{\pi}{2}D_p\right)e^{j\left(\pi D_\phi+\frac{\pi}{2}(1-D_p)+\frac{\pi}{2}\right)},\end{aligned} \tag{18}$$

$$\frac{\hat{\overrightarrow{v}}_{1n}}{\hat{v}_{test}} = \frac{\hat{d}_\phi}{\hat{v}_{test}}4V_{on}\sin\left(\frac{\pi}{2}D_n\right)e^{j\left(\pi D_\phi+\frac{\pi}{2}(1-D_n)+\frac{\pi}{2}\right)}. \tag{19}$$

Using this result and the phasor transformed resonant circuit, the relationship between the perturbed test voltage $\hat{v}_{test}$ and the tank current is found, which can be separated into its envelope and phase response ($\hat{i}^{d_\phi}_{t,env}/\hat{v}_{test}$ and $\hat{\theta}^{d_\phi}_t/\hat{v}_{test}$). The envelope and phase response are both functions of the unknown term $\hat{d}_\phi/\hat{v}_{test}$. This term is solved for using the following expression for $\hat{i}_{out}/\hat{v}_{test}$, which is nulled to zero by definition of Z_n,

$$\frac{\hat{i}_{out}}{\hat{v}_{test}} = \frac{\hat{i}^{d_\phi}_{out}}{\hat{i}_{t,env}}\frac{\hat{i}^{d_\phi}_{t,env}}{\hat{v}_{test}} + \frac{\hat{i}^{d_\phi}_{out}}{\hat{\theta}_t}\frac{\hat{\theta}^{d_\phi}_t}{\hat{v}_{test}} = 0. \tag{20}$$

Upon solving for the unknown term, it can be back-substituted into the expressions of $\hat{i}^{d_\phi}_{t,env}/\hat{v}_{test}$ and $\hat{\theta}^{d_\phi}_t/\hat{v}_{test}$, which can then be used in the desired expression of Z_n as calculated at the p-port:

$$Z_{n-p-port} = \frac{1}{\frac{\hat{i}^{d_\phi}_{test}}{\hat{i}_{t,env}}\frac{\hat{i}^{d_\phi}_{t,env}}{\hat{v}_{test}} + \frac{\hat{i}^{d_\phi}_{test}}{\hat{\theta}_t}\frac{\hat{\theta}^{d_\phi}_t}{\hat{v}_{test}}}. \tag{21}$$

The analysis was performed in MATLAB and evaluated for steady-state operating points throughout the grid cycle. These results are shown in Fig. 4.

C. Calculation of Z_d

To calculate Z_d, a similar analysis to that of Z_n is utilized with the difference that the input variable is set to zero, as in (16). Since all other inputs are zero, the only perturbation is that of $\hat{v}_{test}$ added to V_{po} or V_{on} when Z_d is calculated at the p-port or n-port, respectively. Thus for Z_d measured at the p-port, the relevant tank voltage relationship is

$$\frac{\hat{\overrightarrow{v}}_{1p}}{\hat{v}_{test}} = \frac{4}{\pi}\sin\left(\frac{\pi}{2}D_p\right)e^{j\left(\pi D_\phi+\frac{\pi}{2}(1-D_p)\right)}, \tag{22}$$

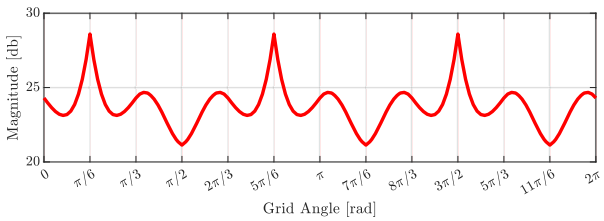

Fig. 4: Magnitude of $Z_{n-p-port}$ at input filter resonant frequency f_{LC} for $G_{old} = \hat{i}_{out}/\hat{d}_\phi$ using small-signal phasor modeling.

and for Z_d measured at the n-port, the tank voltage relationship is

$$\frac{\hat{\overrightarrow{v}}_{1n}}{\hat{v}_{test}} = \frac{4}{\pi}\sin\left(\frac{\pi}{2}D_n\right)e^{j\left(\pi D_\phi+\frac{\pi}{2}(1-D_n)\right)}. \tag{23}$$

Once again, this tank voltage is used with the phasor transformed circuit elements to find the tank current response from the input voltage perturbation, which is separated into its envelope and phase response.

Finally, using the relationship between the p-port current and the perturbed tank envelope and phase, the final expression for Z_d calculated at the p-port is

$$Z_{d-p-port} = \frac{1}{\frac{\hat{i}^{i_{t,env}}_p}{\hat{i}_{t,env}}\frac{\hat{i}^{v_{test}}_{t,env}}{\hat{v}_{test}} + \frac{\hat{i}^{\theta_t}_p}{\hat{\theta}_t}\frac{\hat{\theta}^{v_{test}}_t}{\hat{v}_{test}}}, \tag{24}$$

and when calculated at the n-port is

$$Z_{d-n-port} = \frac{1}{\frac{\hat{i}^{i_{t,env}}_n}{\hat{i}_{t,env}}\frac{\hat{i}^{v_{test}}_{t,env}}{\hat{v}_{test}} + \frac{\hat{i}^{\theta_t}_n}{\hat{\theta}_t}\frac{\hat{\theta}^{v_{test}}_t}{\hat{v}_{test}}}. \tag{25}$$

The calculation of Z_d was performed using MATLAB for all operating points in a grid cycle. The analysis was also compared to a PLECS Blockset multitone analysis, and the results are shown in Fig. 5. Additionally, Fig. 6 shows the bode plot of $Z_{d-p-port}$ at the specific grid angle of $\pi/3$ radians.

D. Impact of LC Resonance Using EET

Without damping, the infinite magnitude of Z_{LC} at f_{LC} interacts with the magnitude of Z_n and/or Z_d, as shown in Fig. 7(a) for the transfer function $\hat{i}_p/\hat{d}_p$ (recall Z_n is infinite for this transfer function). As indicated in (13), the interaction of these magnitudes results in G_{cf} deviating from unity, affecting the plant transfer function G_{old}. This is shown in Fig. 7(b) as an additional 360° phase shift. This phase shift reduces the open-loop phase angle at the desired crossover frequency, which causes instability with closed-loop control bandwidths above the LC resonant frequency.

IV. Damping Filter Design

Whereas an undamped LC circuit has theoretically infinite impedance at resonance, it is desirable to determine the magnitude of Z_n and Z_d at the resonant frequency to know to what extent the resonance must be damped, thus satisfying (14). As seen in Figs. 4 and 5, these magnitudes change depending on the large-signal operating point, which varies throughout

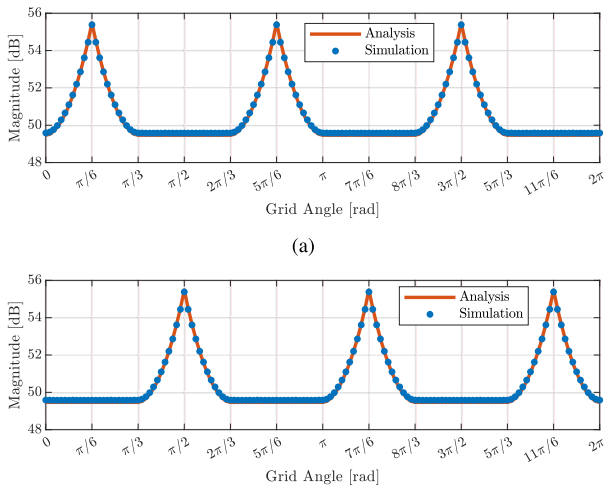

Fig. 5: Comparison of small-signal phasor modeling to PLECS Blockset/MATLAB simulation showing magnitude of (a) $Z_{d-p-port}$ and (b) $Z_{d-n-port}$ at input filter resonant frequency f_{LC}.

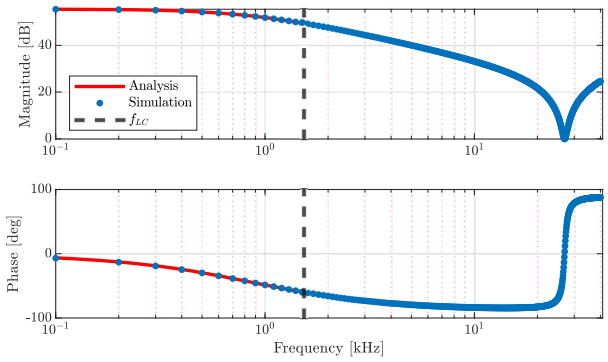

Fig. 6: Comparison of small-signal phasor modeling to PLECS Blockset/MATLAB simulation showing bode plot of $Z_{d-p-port}$ at steady-state operating point of grid angle equal to $\pi/3$ radians.

the grid cycle. The minimum magnitude of $Z_{n-p-port}$ (for transfer function $\hat{i}_{out}/\hat{d}_{\phi}$) is 21.1 dB at grid angle of $\pi/2$ radians (see Fig. 4). The minimum magnitude of $Z_{d-p-port}$ and $Z_{d-n-port}$ (for all transfer functions) is 49.5 dB at grid angle of $\pi/3$ radians (see Fig. 5). These worst case magnitudes are the maximum value to which Z_{LC} must be damped to sufficiently meet the requirements in (14).

For the present application, the LC impedance was damped to >20 dB (i.e., 1/10) below the 49.5 dB of Z_d. The impedance Z_d was prioritized as the damping limit even though it has a greater minimum than Z_n because it impacts the correction factor G_{cf} for all transfer functions, while Z_n is only finite for the transfer function $\hat{i}_{out}/\hat{d}_{\phi}$, which is the transfer function most directly impacting the output power control loop. The output power control loop has a bandwidth below the LC resonant frequency, while the PFC control loop utilizes high-bandwidth control, so the design allows for Z_{LC} to approach Z_n near the resonant frequency.

The chosen resistor value to meet the damping requirements is $R_{damp} = 10\ \Omega$, which corresponds to 20 dB. This value of

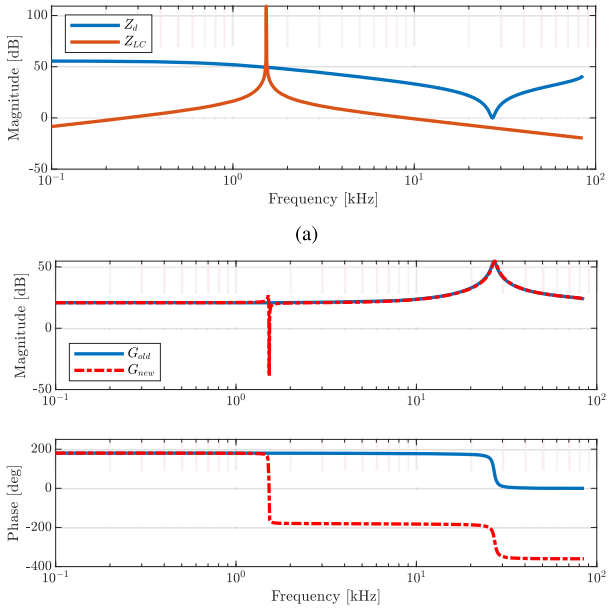

Fig. 7: (a) Comparison of Z_{LC} and Z_d as measured at the p-port for the $\hat{i}_p/\hat{d}_p$ transfer function and (b) the change in the transfer function due to the interaction of Z_{LC} and Z_d seen in (a), which includes a magnitude spike and 360° phase shift at the LC resonant frequency.

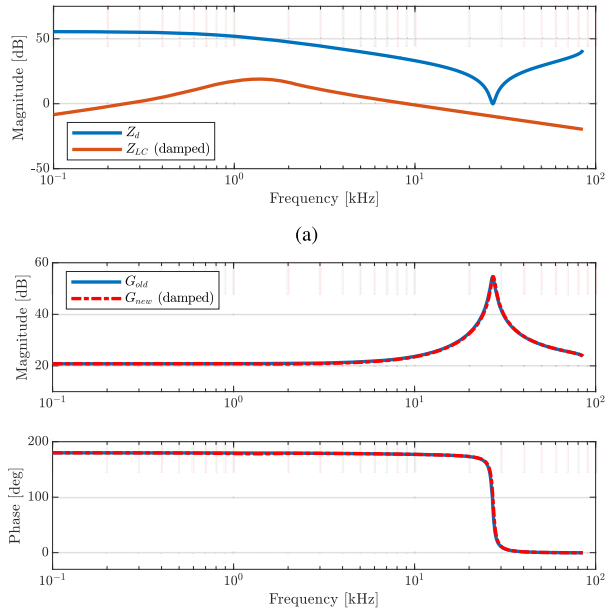

Fig. 8: (a) Comparison of damped Z_{LC} and Z_d as measured at the p-port for the $\hat{i}_p/\hat{d}_p$ transfer function and (b) the change in the transfer function due to G_{cf}. Because Z_{LC} does not interact with Z_d, G_{new} closely matches G_{old}.

R_{damp} is deliberately kept 20 dB lower than the lowest value of Z_d to avoid any interaction between the two impedances Z_d and Z_{LC}. To minimize the power loss at the 60 Hz grid frequency, an additional inductor and capacitor are added in parallel and series, respectively, with the resistor, as shown in the single-phase equivalent diagram in Fig. 9. The series

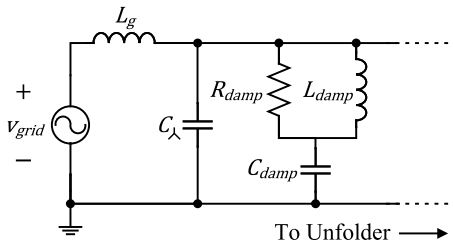

Fig. 9: Single-phase equivalent circuit of input to unfolder, including damping circuit.

capacitor C_{damp} minimizes the total current flow at low frequencies in the damping circuit branch, and the inductor L_{damp} allows low frequency current to bypass the R_{damp} branch specifically. Also, the inductor L_{damp} is chosen such that it has a higher impedance than R_{damp} at f_{LC} to ensure that Z_{LC} is damped to the chosen value of R_{damp}. For the same reason, C_{damp} is chosen to have a lower impedance than R_{damp} at f_{LC}.

With the selected damping filter component values, Z_{LC} now has a peak magnitude of 19.14 dB, thereby not interacting with Z_d. Thus, the requirements in (14) are met, and G_{cf} remains near unity at all frequencies and dc operating points. This is shown in Fig. 8, which shows the same Z_{LC} and Z_d plots as Fig. 7, but with the designed input damping filter.

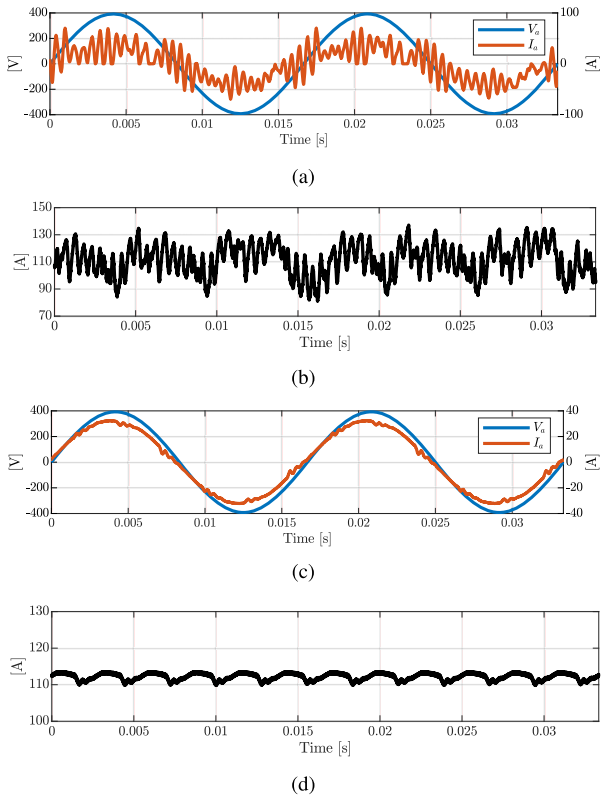

Fig. 10: (a) Phase A voltage and current and (b) output current when the damping filter is disconnected. Waveforms show high THD and distortion. (c) Phase A voltage and current and (d) output current with the damping filter connected, resulting in lower THD and closed-loop stability.

TABLE I: Summary of operating point and component values for simulation and hardware validation.

Parameter	Description
Nominal input voltage (V_{ll})	480 V, 60 Hz
Nominal battery (output) voltage (V_{bat})	160 V
Output power	18 kW
Grid inductance (L_g)	600 μH
Soft-dc-link capacitance ($C_{po/on/pn}$)	6.024 μF
Reflected grid-side capacitance ($C_{\curlywedge}$)	18.072 μF
L_g to $C_{\curlywedge}$ resonant frequency (f_{LC})	1.53 kHz
Unfolder diode ($D_{a1/b1/c1/a2/b2/c2}$)	WT1263Y200, 2000 V, 1263 A
Unfolder back-to-back IGBT ($Q_{a/b/c}$)	FZ1200R17KF6C-B2, 1700 V, 1200 A
T-SRC primary H-bridge MOSFET ($Q_{x1/y1/x2/y2}$)	GeneSiC G3R30MT12K 1200 V, 50 A, 2 in parallel
T-SRC back-to-back MOSFET ($Q^{-}_{x3/y3}$, $Q^{+}_{x3/y3}$)	GeneSiC G3R30MT12K 1200 V, 50 A
T-SRC secondary MOSFET ($Q_{u1/v1/u2/v2}$)	Infineon IRFP4768PBF 250 V, 93 A, 2 in parallel
T-SRC switching frequency (f_s)	93.3 kHz
Transformer turns ratio (n_t)	0.25
Resonant inductance (L_s)	48 μH
Resonant capacitance (C_s)	120 nF
Output capacitance (C_{out})	195.2 μF
Damping resistance (R_{damp})	10 Ω
Damping inductance (L_{damp})	2.5 mH
Damping capacitance (C_{damp})	25 μF

V. Simulation and Experimental Validation

To validate the proposed damping technique, simulations using PLECS were ran with and without the damping filter. Table I shows the operating point and component values used in the simulation. The results, shown in Fig. 10, show high total harmonic distortion (THD) and poor PFC and output power regulation when the input impedance is not damped (Figs. 10(a) and (b)) and significantly improved waveforms with the damping filter included (Figs. 10(c) and (d)).

Additionally, the simulation was used to investigate the impact on the converter's efficiency when the damping filter is included. In steady-state operation, the simulation showed the shunt damper sinking an average of 4.24 W of power. With a rated output power of 18 kW, and a peak simulated efficiency of 97.9%, the shunt damper contributes a maximum of 1.09% of the system losses, or a 0.023% reduction in efficiency.

The system was tested in hardware using the setup shown in Fig. 11 and the same values as in Table I. As shown in Fig. 11,

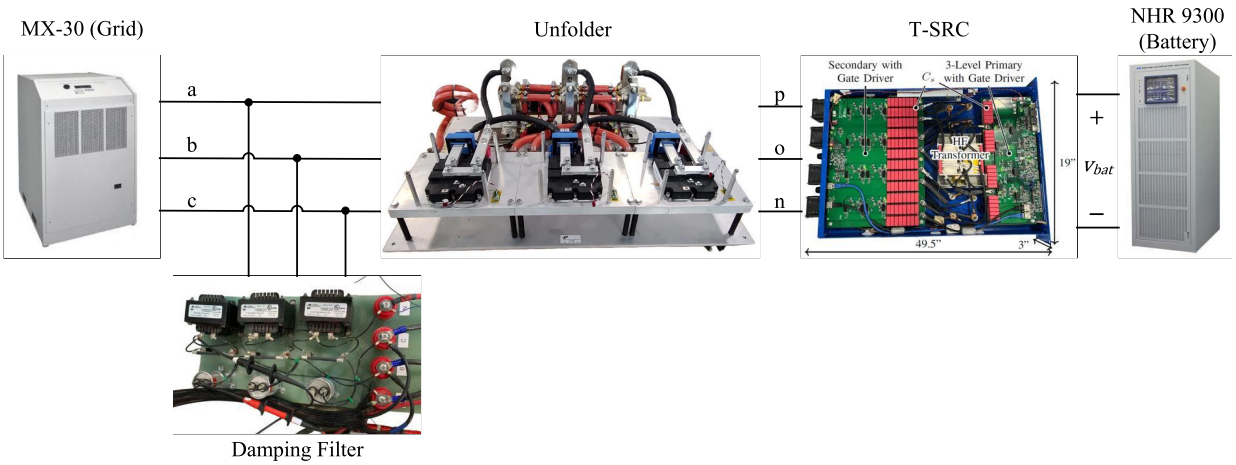

Fig. 11: Block diagram of hardware setup for T-SRC with the damping filter at input.

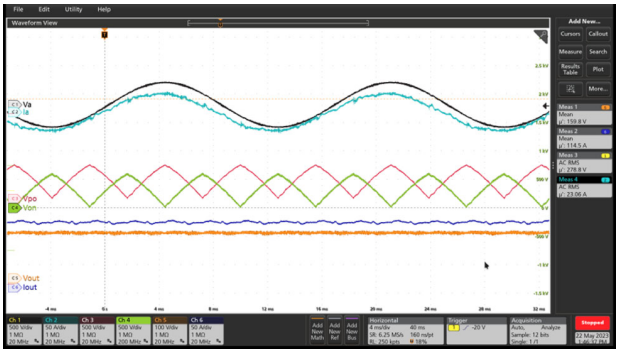

Fig. 12: Oscilloscope capture of input and output waveforms. Waveform colors correspond with the following signals: black is V_a voltage, cyan is I_a current, pink is V_{po} voltage, green is V_{on} voltage, blue is battery current, and orange is battery voltage.

the testing assembly comprises a California Instruments MX-30 as a three-phase grid emulator, an unfolder, an 18 kW T-SRC module, and an NH Research 9300 in battery mode as the battery emulator. Connected in parallel to the three-phase input is the damping filter described in Section IV. With the damping filter connected, the converter can utilize a PFC control loop bandwidth greater than the LC resonant frequency without becoming unstable, as shown in Fig. 12.

VI. Conclusion

To conclude, this paper shows the effect of the resonance due to the equivalent input filter made from grid inductance and the dc-link capacitance of a three-phase ac-dc converter. First, the small-signal phasor modeling of the converter is explained, and three key transfer functions impacting the PFC and output power control loop are presented. Using similar modeling techniques, the EET impedances Z_n and Z_d of each transfer function are derived. Knowing the minimum magnitude of the EET impedances, a damping filter is designed to lower the peak magnitude of Z_{LC}. With the proposed damping filter, the three plant transfer functions are not affected, thereby allowing PFC closed-loop operation above the LC resonant frequency. The proposed damping filter is validated in both simulation and hardware experimentation. The experimentation results indicate significant distortion without the damping filter and reduced grid current THD with the damping filter. This is accomplished with only a very minor (0.023%) reduction in converter efficiency.

References

[1] O. A. A. Amer, I. Abdelsalam, and M. I. Marei, "An ev on-board charger based on dual-boost ac-dc converter," in *2024 International Telecommunications Conference (ITC-Egypt)*, 2024, pp. 263–268.

[2] R. Dwivedi, S. Singh, B. Singh, A. Chandra, and M. Rezkallah, "Three-phase ac/dc converter fed two parallel interleaved dc-dc converters for fast charging applications with improved power quality," in *2023 IEEE 14th International Conference on Power Electronics and Drive Systems (PEDS)*, 2023, pp. 1–6.

[3] L. Schrittwieser, J. W. Kolar, and T. B. Soeiro, "Novel swiss rectifier modulation scheme preventing input current distortions at sector boundaries," *IEEE Transactions on Power Electronics*, vol. 32, no. 7, pp. 5771–5785, 2017, doi: 10.1109/TPEL.2016.2609935.

[4] M. A. Mansour, "Control development for a medium-voltage three-phase unfolding input-series-output-parallel ac-dc converter," M.S. thesis, Utah State University, Logan, UT, May 2022, available at https://digitalcommons.usu.edu/etd/8475.

[5] A. Zade, S. Gurudiwan, D. Maksimović, and R. Zane, "High-bandwidth control of a 20-kw single-stage unfolding-based ac-dc converter using the extra element theorem and current emulation technique," *IEEE Transactions on Power Electronics*, pp. 1–19, 2024, doi: 10.1109/TPEL.2024.3423705.

[6] X. Li, J. Sun, L. Guo, M. Gao, H. Hu, and M. Xu, "A three-phase single-stage ac/dc converter based on swiss rectifier and three-level llc topology," *IEEE Transactions on Power Electronics*, vol. 38, no. 2, pp. 1958–1972, 2023.

[7] S. Gurudiwan, R. Hatch, M. Mansour, H. Wang, and R. Zane, "An 18 kw battery charger module for extreme fast charging applications using an unfolding-based ac-dc topology," in *2023 IEEE Applied Power Electronics Conference and Exposition (APEC)*, 2023, pp. 1715–1722, doi: 10.1109/APEC43580.2023.10131542.

[8] K. Kroics and J. Zarembo, "Lc input filter passive damping improvement for traction drive application," in *2021 IEEE 2nd International Conference on Smart Technologies for Power, Energy and Control (STPEC)*, 2021, pp. 1–4.

[9] P. N. A. Megat Yunus, A. Jusoh, and M. K. Hamzah, "Passive damping network for a single phase matrix converter (spmc) operating as a rectifier," in *2011 IEEE Symposium on Industrial Electronics and Applications*, 2011, pp. 173–177.

[10] C. Rim and G. Cho, "Phasor transformation and its application to the dc/ac analyses of frequency phase-controlled series resonant converters (src)," *IEEE Transactions on Power Electronics*, vol. 5, no. 2, pp. 201–211, 1990, doi: 10.1109/63.53157.

[11] D. Seltzer, L. Corradini, D. Bloomquist, R. Zane, and D. Maksimović, "Small signal phasor modeling of dual active bridge series resonant dc/dc converters with multi-angle phase shift modulation," in *2011 IEEE Energy Conversion Congress and Exposition*, 2011, pp. 2757–2764, doi: 10.1109/ECCE.2011.6064139.

[12] R. W. Erickson and D. Maksimovic, "Techniques of Design-Oriented analysis: Extra element theorems," in *Fundamental of Power Electronics*, 3rd ed. Cham, Switzerland: Springer, 2020, ch. 16, pp. 625–632.

[13] R. Middlebrook, "Null double injection and the extra element theorem," *IEEE Transactions on Education*, vol. 32, no. 3, pp. 167–180, 1989, doi: 10.1109/13.34149.

[14] ——, "The two extra element theorem," in *Proceedings Frontiers in Education Twenty-First Annual Conference. Engineering Education in a New World Order*, 1991, pp. 702–708, doi: 10.1109/FIE.1991.187583.

[15] R. Middlebrook, V. Vorperian, and J. Lindal, "The n extra element theorem," *IEEE Transactions on Circuits and Systems I: Fundamental Theory and Applications*, vol. 45, no. 9, pp. 919–935, 1998, doi: 10.1109/81.721258.